Geophysical Research Letters

RESEARCH LETTER
10.1029/2019GL082485

Ice Thickness and Bed Elevation of the Northern and Southern Patagonian Icefields

R. Millan[1,2], E. Rignot[1,3,4], A. Rivera[5,6], V. Martineau[1], J. Mouginot[1,2], R. Zamora[6], J. Uribe[6], G. Lenzano[7], B. De Fleurian[8], X. Li[1], Y. Gim[3], and D. Kirchner[9]

[1]Department of Earth System Science, University of California, Irvine, CA, USA, [2]Université Grenoble Alpes, CNRS, IRD, Grenoble INP, IGE, Grenoble, France, [3]Jet Propulsion Laboratory/Caltech, Pasadena, CA, USA, [4]Centro de Estudios Científicos, Valdivia, Chile, [5]Departamento de Geografia, Universidad de Chile, Santiago, Chile, [6]Centro de Estudios Científicos, Valdivia, Chile, [7]Departamento de Geomatica, Instituto Argentino de Nivologia, Glaciologia y Ciencias Ambientales (IANIGLA), Centro Científico y Tecnoligico (CCT)-CONICET, Mendoza, Argentina, [8]Bjerknes Center for Climate Research, University of Bergen, Bergen, Norway, [9]Department of Physics and Astronomy, The University of Iowa, Iowa City, Iowa, USA

Abstract The Northern and Southern Patagonian Icefields are the largest ice masses in the Southern Hemisphere outside Antarctica, but their ice volume and bed topography are poorly known. Here, we combine airborne gravity data collected in 2012 and 2016, with radar data from the Warm Ice Experiment Sounder and Centro de Estudios Científicos's to map bed elevation and ice thickness in great detail. We perform a 3-D inversion of the gravity data constrained by radar-derived thickness and fjord bathymetry to infer bed elevation at 500-m spacing, with a precision of about 60 m. We detect deep glacial valleys with ice thickness exceeding 1,400 m and sectors below sea level on the western branch of Glaciar Pio XI, Occidental, between San Rafael and Colonia, and near Fitz Roy. We calculate an ice volume of 4,756 ± 923 km^3 for Northern Patagonia Icefield and Southern Patagonia Icefield, or 40 times the volume of glaciers in the European Alps.

Plain Language Summary Traditional techniques of radar depth sounding fail to resolve thick, temperate ice masses due to poor penetration of the radar signals into snow and ice and extensive scattering due to water content. We combine sparse airborne radar sounding and bathymetry data with novel high-resolution, high-precision airborne gravity data to infer the bed topography of the Patagonia Icefields of South America. The results reveal the full range of deep ice thickness on the plateau, portions of the icefields grounded below sea level, and the total volume content of the Patagonia Icefields. The results are critical to constrain the details of the past, present, and future evolution of this glaciated region in a warmer climate.

Key Points:
- Comprehensive ice thickness and bed elevation measurements are conducted on the Northern and Southern Patagonian Icefields of South America
- Ice thickness in excess of 1,400 m is observed over selected regions of the plateau
- A multisensor approach solves the problem of mapping the thickness of temperate ice masses

Supporting Information:
- Supporting Information S1

Correspondence to:
R. Millan,
millanr1@uci.edu

Citation:
Millan, R., Rignot, E., Rivera, A., Martineau, V., Mouginot, J., Zamora, R., et al. (2019). Ice thickness and bed elevation of the Northern and Southern Patagonian Icefields. *Geophysical Research Letters*, *46*, 6626–6635. https://doi.org/10.1029/2019GL082485

Received 21 FEB 2019
Accepted 4 MAY 2019
Accepted article online 3 JUN 2019
Published online 17 JUN 2019

1. Introduction

The Patagonian Icefields covered an area of 13,219 km^2 for the Southern Patagonia Icefield (SPI) and 3,976 km^2 for the Northern Patagonia Icefield (NPI) in 2011 (Davies & Glasser, 2012). Together, they represent the largest ice mass in the Southern Hemisphere outside Antarctica. This region experiences exceptional precipitation levels of several meters per year on its western flank (Lenaerts et al., 2014) and hosts some of the fastest moving glaciers in the world, moving up to 10 km/year (Mouginot & Rignot, 2015). Time series of surface elevation data from satellite radar altimetry and optical imagery have shown that all the glaciers, except for Glaciares Pio XI and Moreno, have thinned rapidly in the last 40 years, with a contribution to sea level rise of 0.042 ± 0.002 mm/year between 1968 and 1975–2000 (Rignot et al., 2003), 0.067±0.004 mm/year during 2000–2012 (Willis et al., 2012), and 0.059 ± 0.005 mm/year during 2011–2017 (Foresta et al., 2018). However, accurate observation of the icefield volume is lacking. Using a perfectly plastic model, Carrivick et al. (2016) estimated a volume of ice of 4,326 ± 865 km^3 for SPI and 1,234 ± 247 km^3 for NPI. Other simple models, based on Glen's flow law and empirical relationships, estimated a total volume of the Patagonian Icefields of 4,607 ± 1.2 km^3 (Farinotti et al., 2019). There are, however, few data to evaluate these models, and it is not clear that these models have skills at reproducing subtile details of the spatial variation in ice thickness within glaciers and ice fields. The lack of precise bed elevation and thickness data therefore limits our ability to quantify the potential contribution to sea level by this region,

model glacier dynamics in response to climate change, or study the impacts of climate change on freshwater resource management and natural hazards such as lake outburst floods (Loriaux & Casassa, 2013).

In 2012, we mapped ice thickness over 49% of NPI and 30% of SPI using the Sander Geophysics Ltd.'s Airborne Inertially Referenced Gravimeter (AIRGrav) gravimeter on an helicopter (Gourlet et al., 2016). Some of the largest glaciers systems in Patagonia, for example, Pio XI, Viedma, or Upsala, were not included in the survey, leaving more than 11,400 km^2 or 65% of NPI and SPI unknown. In 2014, we conducted an extensive survey of the SPI using the Warm Ice Experiment Sounder (WISE) radar sounder (Rignot et al., 2013). In 2014–2015, the Centro de Estudios Cientificos (CECs) in Valdivia flew a 20-MHz radar sounder to map ice thickness (Zamora & Uribe, 2017) in SPI. In 2016, we completed a second gravity survey of the remainder of the NPI and the central and southern SPI using AIRGrav on a fixed-wing aircraft. Here, we present a three-dimensional inversion of the combined 2012 and 2016 airborne gravity data, constrained by the 2014 WISE and 2014–2015 CECs data, along with lake and fjord bathymetry, to extend the mapping of ice thickness and bed elevation significantly in coverage and quality over NPI and SPI. We discuss the results and their impact on our understanding of the past, present, and future evolution of the NPI and SPI.

2. Data and Methods

Gravity data. In May and November 2012, the AIRGrav system was deployed onboard an AS-350 helicopter to measure gravity anomalies in the NPI and northern SPI (Gourlet et al., 2016). An emphasis was placed on a dense line spacing (500 m) for the outlet glaciers versus the plateau (2-km line spacing). Using this survey and surveys conducted in Greenland (An et al., 2017), we determine that maintaining a low elevation above ground was more important than maintaining a low speed to capture gravity anomalies associated with glacial troughs. A follow-on survey was organized on a fixed-wing aircraft, which lowered the cost and safety requirements. We also found that mapping narrow, deep, terminal glacier valleys was more challenging than mapping the plateau because valleys required rapid changes in plane altitude, tighter line spacing, and lower safety levels. In addition, a novel method of ice thickness mapping using mass conservation combining sparse thickness data with ice flow vectors had emerged in the interim (Morlighem et al., 2014). The mass conservation method is most efficiently applied at lower elevation, with high flow speed, low errors in flow direction, and greater availability of radar ice thickness data to constrain the gravity inversion, hence placing more importance on the need to survey the upper reaches of the icefields with gravity rather than the lower reaches.

In July 2016, we deployed AIRGrav on a low flying, fixed-wing aircraft for 3 weeks to survey the remainder of NPI between San Quintin and Steffen glaciers, and the central and southern parts of the SPI plateau south of Glaciar O'Higgins (Figure S1 in the supporting information). We used a Cessna-206 aircraft and split the survey into seven flights between 22 July to 1 August 2016 from Villa O'Higgins, Chile, at the foothills of SPI (Figure S1). AIRGrav has draping capabilities, which enables data collection with changes in altitude, direction, or shallow-bank turns. We optimized the survey by avoiding high mountain ranges with steep slopes, where ice thickness is low, to minimize changes in altitude, maintain the safety of the survey, and maximize data quality. The traverse line spacing was 2 km, with a target speed of 80 knots and a ground clearance of 100 m. Control line were placed so that intersections area could be maximize and terrain clearance could be maintained.The gravity anomalies were recorded at 128 Hz with a nominal noise level of 0.2 mGal. The data were corrected for the Eotvos, normal, free-air, and static effects. Statistical noise was reduced using a 20-s half-wavelength filter. The 2012 and 2016 free-air gravity anomalies were merged onto a 500-m grid and low-pass filtered using a 1,250-m half-wavelength (Figure 1). Data noise of the final product was less than 1 mGal. In 2012, the helicopter carried a laser altimeter with a submeter vertical precision. In 2016, we used a TRA-3500 radar altimeter system to provide above ground altitude information with an accuracy of 5% to 7%. Data gaps on the eastern part of Jorge Montt glacier (Figures 1 and S1) were due to weather and time limitations.

WISE radar sounder. Ice thickness was surveyed using the Jet Propulsion Laboratory/University of California Irvine WISE radar sounder (Rignot et al., 2013; Mouginot et al., 2014) in November 2014 (Figure S2) onboard a Piper Seneca aircraft with tone waveforms at a pulse repetition frequency of 1-kHz, 2.5-MHz center frequency, with 1-μs duration pulses (Figure S2). A conventional GPS receiver was operated at 10 Hz with a vertical precision of 10 m. We recorded radar data between 150 and 300 m above the ice surface. Low-altitude flying increases spatial resolution and clips radar returns from the surface, which reduces data

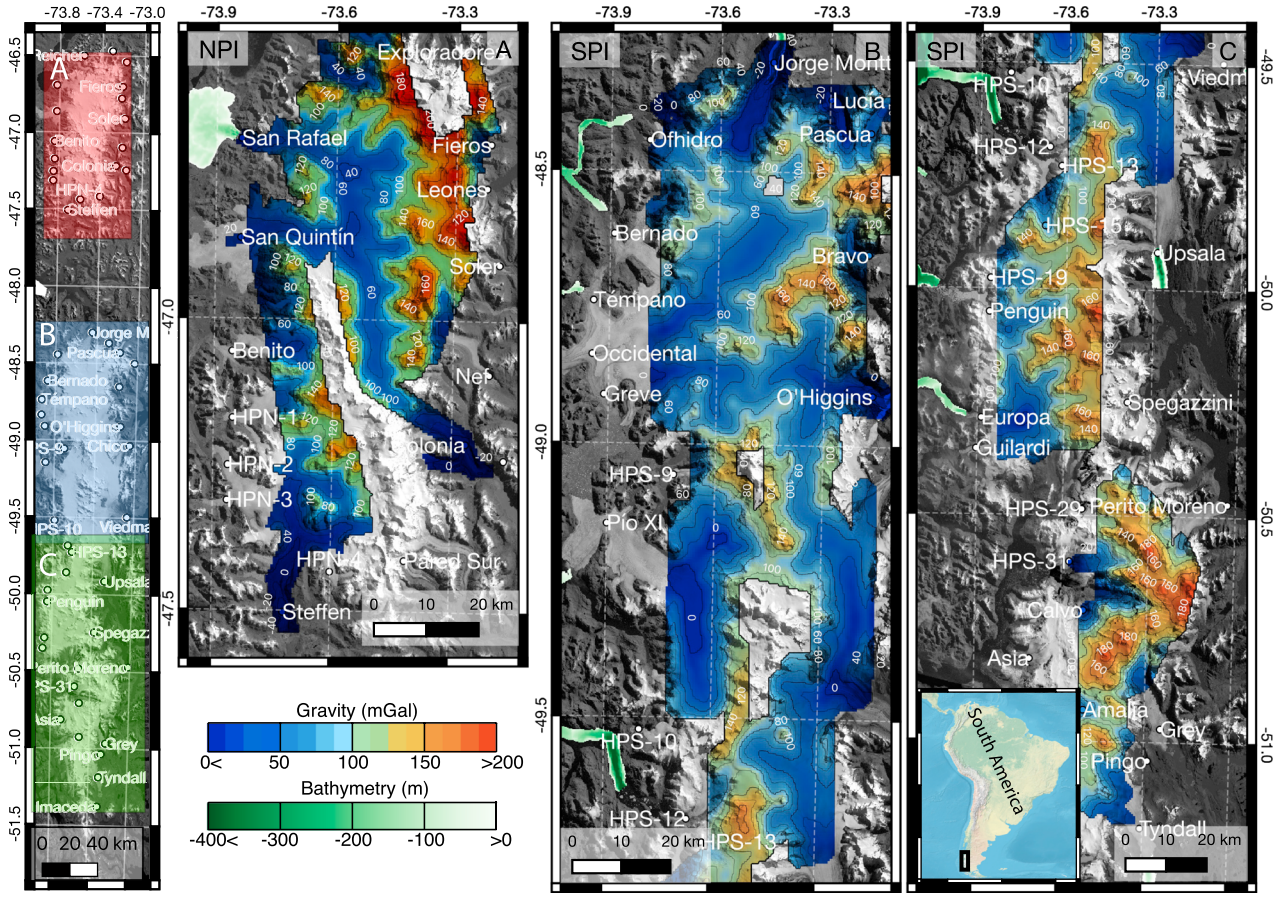

Figure 1. Free-air gravity anomalies color coded from blue to red in (a) NPI, (b) northern SPI, and (c) southern SPI overlaid on a Landsat 7 image mosaic from 2001 to 2003. Fjord and lake bathymetry measurements are in shaded relief on a color scale ranging from dark green (deep) to light green (shallow). A location map is shown on the left panel. Inset is showing a global location map of the studied region. NPI = Northern Patagonia Icefield; SPI = Southern Patagonia Icefield.

clutter (Mouginot & Rignot, 2015). We deduced ice thickness from the difference between a reference surface elevation from a TanDEM-X digital elevation model (DEM) from year 2015 and bed elevation measured from the WISE radar echograms. We employed a constant dielectric of 3.15 for ice and apply no firn correction. Even with the low-altitude flight, the separation of off-nadir and bed returns was ambiguous. To assist in the identification of bed versus surface returns, we used a radar simulation where the surface is decomposed into facets (larger than the radar wavelength) and each facet is treated as a quasi-specular reflector (Nouvel et al., 2004; Rees, 1990; Ulaby et al., 1982). We calculated the overall return from the facets as a function of facet orientation and distance from the radar. We neglected interferences that occurred in the signal and used the simulation in a qualitative way to interpret the WISE echograms. Bed returns were digitized manually and classified with a quality flag that reflected the uncertainty of identification of the bed: Quality 0 = 100 m, 1 = 50 m, and 2 = 25 m (Figure S3).

CECs radar sounder. The CECs is controlled and operated from a computer inside a helicopter cabin, which is connected with an optical fiber cable to the main antenna structure, this latter weighting 350 kg and hanging 40–50 m below the helicopter (Blindow et al., 2012). The radar is an impulse system operating at 20 MHz of central frequency. At the antenna structure, a 3.2-kV high-power transmitter operated at 3 kHz of pulse repetition frequency is installed, in addition with the radar receiver. A dual frequency GPS was used for precise location of the radar measurements. The survey took place August–September 2014 and September–October 2015 over more than 400 km of measurements in Jorge Montt, O'Higgins, and the high plateau of SPI (Figure S6). The system performance was adequate to survey most of the ice thickness, including steep slopes and inaccessible crevassed areas. The maximum measured ice thickness was 581 m. Several bottom reflections were obscured by englacial water and/or surface crevasses. Ice thickness was calculated

assuming an electromagnetic wave speed of 0.168 m/ns in ice (Zamora & Uribe, 2017). In addition, we used radar data from other sources (Raymond et al., 2005; Rivera & Cassassa, 2002; Zamora & Uribe, 2017; Figure S3). Error were estimated by analyzing crossing profiles and evaluated to be 6% of the thickness.

Bathymetry. The inversion of gravity data over open water is constrained by lake and fjord bathymetry data where available (Figures 1 and S3). We use fjord bathymetry for Glaciar Jorge Montt by Rivera et al. (2012) collected with a sonar system and a Datasonic Bubble Pulser subbottom profiler. For Lake O'Higgins, Casassa et al. (2007) collected bathymetry data using a parametrical echo sounder (Innomar) in 2004 and 2005. We integrate bathymetry from Koppes et al. (2010) for Laguna San Rafael collected on a zodiac using a Datasonics Bubble Pulser combined with a Lowrance 18-C depth sounder (Koppes et al., 2010). Finally, we use data from Glaciar Tyndall (Raymond et al., 2005), Upsala (A. Rivera, personal communication, 2018), HPS-12, Bernardo, Tempano, and Pio XI (Dowdeswell & Vasquez, 2013). All bathymetry data have a vertical resolution that is better than 10 m (Casassa et al., 2007; Dowdeswell & Vasquez, 2013; Koppes et al., 2010).

Gravity inversion. We form a 3-D model of NPI and SPI using the Geosoft GMSYS-3D software package, which implements Parker's (1973) standard method. The 3-D model includes three layers with densities of 0.917 g/cm^3 for ice, 1.028 g/cm^3 for water, and 2.67 g/cm^3 for bedrock. For surface reference, we use the 2012 laser altimeter data along the 2012 surveys and a combination of TanDEM-X from year 2015 (10-m spacing) and year 2000 SRTM (30-m spacing) for the 2016/2017 surveys. We correct for changes in elevation between 2000 and 2012–2016 using a linear interpolation for regions with an overlap with TanDEM-X. In contrast with Gourlet et al. (2016), we do not upward continue the gravity data to 3,000-m elevation, as this approach smears out gravity anomalies, reduces data resolution and the depth of the inferred bed troughs. Instead, we process the 2012 and 2016 gravity data at their own elevation, with minimal impact on data resolution, at the expense of longer calculations (Millan et al., 2018). To account for changes in gravity caused by geology below the modeled domain, we constrain the gravity inversion with observations from radar sounder, bathymetry, and elevation of exposed rock outcrops as in An et al. (2019). Using a preliminary solution of the bed topography that combines (1) radar (WISE Q1,Q2, and CECs), (2) bathymetry, and (3) rock outcrops. Where none of the previous data are available, the grid is completed with a scaled version of the gravity signal, where the scaling factor is the average ratio between observed and calculated gravity where we have in situ data (1–3). Using this initial solution, we formulate a forward modeling of the gravity field spatially averaged at 500-m resolution. We compare the modeled and observed gravity (the difference is named the DC-shift) over areas where we have reliable data and interpolate the DC-shift over areas with no data using a minimum curvature algorithm (Figure S4). The DC-shift varies with the underlying the geology of the region (An et al., 2019; Hodgson et al., 2019), for example, changes in crustal thickness and layer density associated with tectonic faults and active volcanoes. The results are low-pass filtered to remove short-wavelength variations and added to the observed gravity before the inversion (Millan et al., 2017). During the inversion process, we calculate the gravity from the initial model and compared it to the observed gravity. The initial model is modified iteratively until we obtain the best match with the observed data (An et al., 2019; Millan et al., 2018; Muto et al., 2016; Tinto & Bell, 2011). We calculate the gravity misfit as the difference between modeled and observed gravity anomalies. We quantify the performance of the inversion by comparing the inferred ice thickness with radar-derived thickness data.

3. Results

After the inversion, the difference between modeled and observed gravity is -0.4 ± 3.1 mGal (mean $\pm$ standard deviation; Figure S5). This gravity misfit translates into a root-mean-square error of 53 m in bed elevation if we use a conversion factor of 5.8 mGal per 100 m of ice (An et al., 2017; Millan et al., 2018). The misfit is systematically negative in the trough and positive at the edges of the basins (Figure S5), which suggests that the model underestimates elevation at the center of the glacial valleys and overestimates it on the margins. We also compare the results of the gravity inversion with the radar sounder data (Figure S6). The mean difference and standard deviation between inferred and observed thickness is -22 ± 170 m, -19 ± 164 m, -19 ± 154 m for WISE Q1, WISE Q2, and CECs data, respectively. Overall, the difference with all radar data is -22 ± 159 m. We define the overall uncertainty on our results as the sum of random errors on the ice thickness measurements (gravimeter accuracy and gravity misfit) to be 60 m. When we compare our results with the modeled ice thickness from Carrivick et al. (2016), we find that the Carrivick et al. (2016) results overestimate the bed elevation by 82 ± 290-m relative to our inversion, with differences exceeding 800 m in some areas, especially over deep troughs (Figure S7).

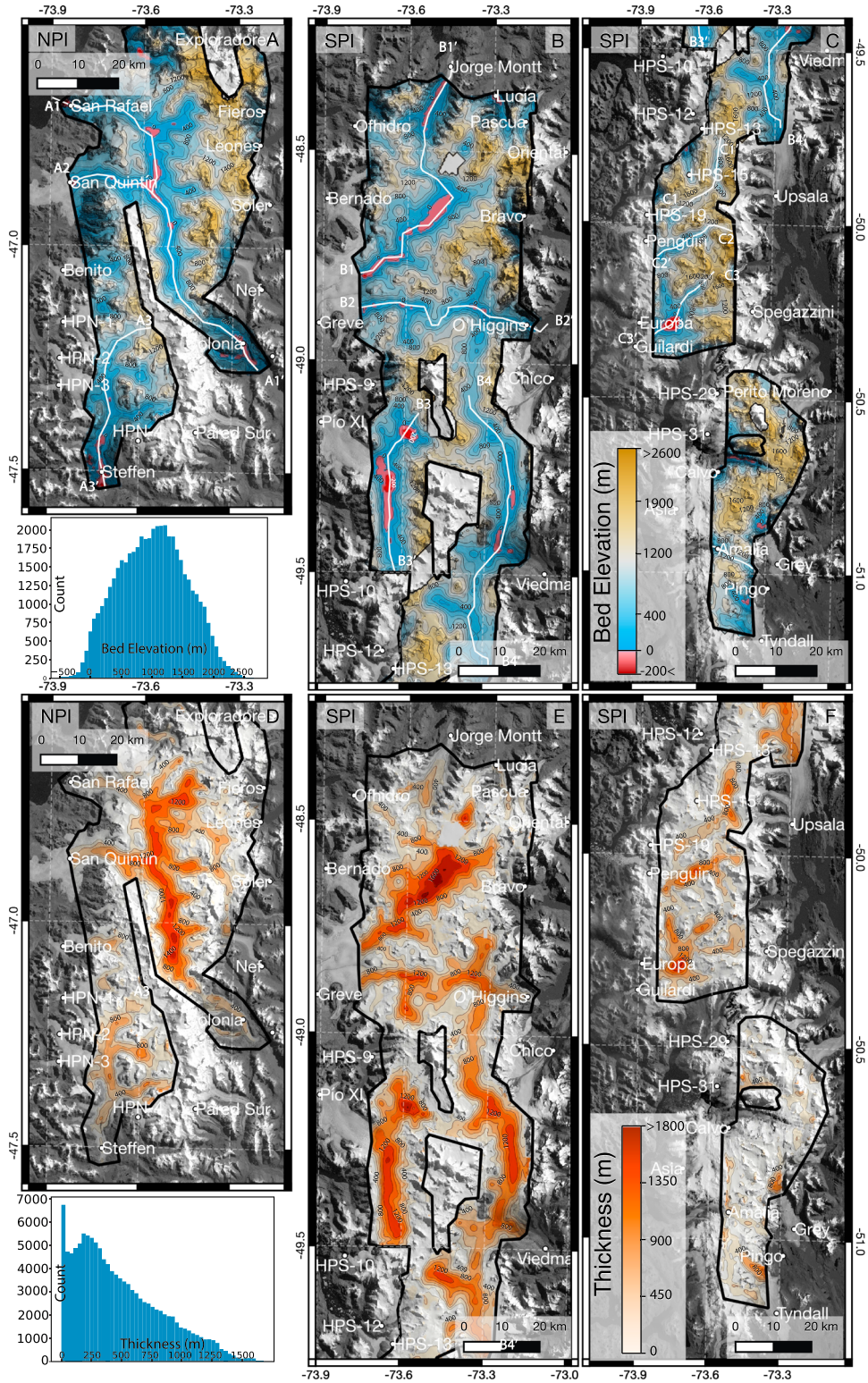

Figure 2. Bed elevation above mean sea level, inferred from the airborne gravity and radar data for (a) NPI, (b) northern SPI, and (c) southern SPI. Calculated ice thickness for (d) NPI, (e) northern SPI, and (f) southern SPI. Contour lines are 200-m contour intervals. Background is a Landsat 7 image mosaic from 2001 to 2003. Areas below sea level are red. Fjord and lake bathymetry is colored from dark red (deep) to light red (shallow) (only a–c panels). Inset includes histograms of (g) bed elevation and (h) ice thickness. NPI = Northern Patagonia Icefield; SPI = Southern Patagonia Icefield.

Our survey completes prior mapping of bed topography in NPI by filling data gaps in the southern and western parts. The new survey reveals more details about major troughs beneath the ice, areas below sea level, and zones of overdeepening. For instance, we find that Glaciar Steffen merges from three branches more than 700 m thick; ice thickness exceeds 700 m on Benito glacier and 900 m on Glaciar San Quíntin 15 km from the ice margin (Figures 2a–2d and 3). In the terminal valley of Glaciar San Rafael and in the upper reaches of Glaciar Steffen, the new bed elevation is several 100 m deeper and exhibit greater spatial variability than in Gourlet et al. (2016) due to the higher-resolution treatment of our new inversion (Figure 3, A1–A1′, A3–A3′). A main feature of NPI is the northwest-southeast trough between San Rafael, San Quíntin, and Colonia glaciers, which connects with the terminal valley of Glaciar San Quíntin, and displays thicknesses up to 1,400 m in central NPI (Figure 3). The inferred bed elevation in this area displays more roughness (Figure 3, A2–A1′, A1–A1′) that in prior mappings.

In SPI, our survey extends from Glaciar Jorge Montt in the north to Glaciar Tyndall at the southern tip (Figure 2). The inferred bed topography beneath Glaciar Jorge Montt agrees with Gourlet et al. (2016) with a mean difference of 60 m but more spatial variability (Figures 2 and 3, B1–B1′). Near Jorge Montt ice fall, we infer a steeper bed slope and shallower bed elevation than in Gourlet et al. (2016). Toward Glaciares Témpano and Occidental, the bedrock is 200 m deeper than in prior mappings, with a succession of sills and troughs (Figure 2). The deepest and widest glacial valleys are observed between Occidental and Pascua, with thickness >1,600 m, and Occidental and O'Higgins, with thickness >1,200 m (Figures 2 and 3, B2–B2′).

This study reveals the southern SPI, south of Volcano Laurato between Glaciar Chico on the east and HPS-9 on the west (Figures 1 and 2). We find the deepest ice in the accumulation area of Glaciar Pio XI with thickness >1,300 m along B3–B3′ and a relatively flat bed (Figures 2 and 3, B3–B3′). On the eastern side of SPI, we find thick ice (>1,400 m) between Chico, Viedma, and O'Higgins glaciers, west of Fitz Roy (Figures 2 and 3, B4–B4′). The upper basin of Glaciar Upsala also hosts ice >1,200 m thick. South of Upsala, ice is typically thinner, but we detect deep glacial valleys beneath Glaciares HPS-13, HPS-15, HPS-19, Penguin, Europa, and Guilardi. The trough between HPS-19 and HPS-13 has thickness >800 m (Figures 2 and 3, C1–C1′). Glaciares Penguin, Europa, and Guillardi host ice up to 1,200–1,400 m at the equilibrium line altitude (Figures 2 and 3), with overdeepenings on Penguin (Figure 3, C2–C2′) and especially Europa (Figure 3, C3–C3′). South of Glaciar Guilardi, SPI is characterized by shallower ice thickness (<500 m) among a rougher and steeper topography (Figure 2), with a high concentration of steep peaks above 2,000-m elevation. The deepest ice is found upstream of Glaciares Tyndall and Grey with thickness of up to 950 m.

We find several areas grounded below sea level: in NPI, the lower reaches of Steffen and San Quíntin, and in the trough connecting San Rafael, San Quíntin, and Colonia, with the deepest ice beneath San Quíntin. In SPI, the lower reaches of Jorge Montt, Lucia, Occidental, Greve, O'Higgins, PioXI, Viedma, Europa, Grey, and Tyndall are below sea level. In total, 267 km^2 of glacier area, or 2.2% of NPI and SPI, is grounded below sea level. All of these basins, however, are protected by higher ground along the periphery, so we find no direct pathway for the rapid retreat of glacier fronts along marine-based channels toward the interior of the icefield. At present, the most vulnerable glacier is Jorge Montt, grounded below sea level for 16 km upstream of the current ice front, which favors retreat due to warm-water-induced melt (Millan et al., 2018; Wood et al., 2018). More data are needed in the lower reach of Occidental and Pio XI to draw conclusions on their vulnerability to warm water intrusions.

Areas exposed to high surface melt production with overdeepenings could host meltwater, which would influence ice dynamics, or create natural hazards. Potential for holding subglacial waters exist on Colonia, which has experienced rapid lake drainage, Of Hidro, which is known for surges, and San Quíntin in NPI. In SPI, overdeepenings exist on Jorge Montt, Occidental, O'Higgins, PioXI, Viedma, Penguin, Europa, and Tyndall.

4. Discussion

The new bed topography improves the results in Gourlet et al. (2016) because of additional gravity, bathymetry, and radar thickness data. In addition, we employ no upward continuity of the gravity data, which maintains a high spatial resolution and preserves the depth of glacial troughs. In comparison with Carrivick et al. (2016), our product reveals more reliable details about the spatial network of subglacial valleys, for example, the trough connecting Occidental and O'Higgins and San Quíntin and Colonia (Figure 2).

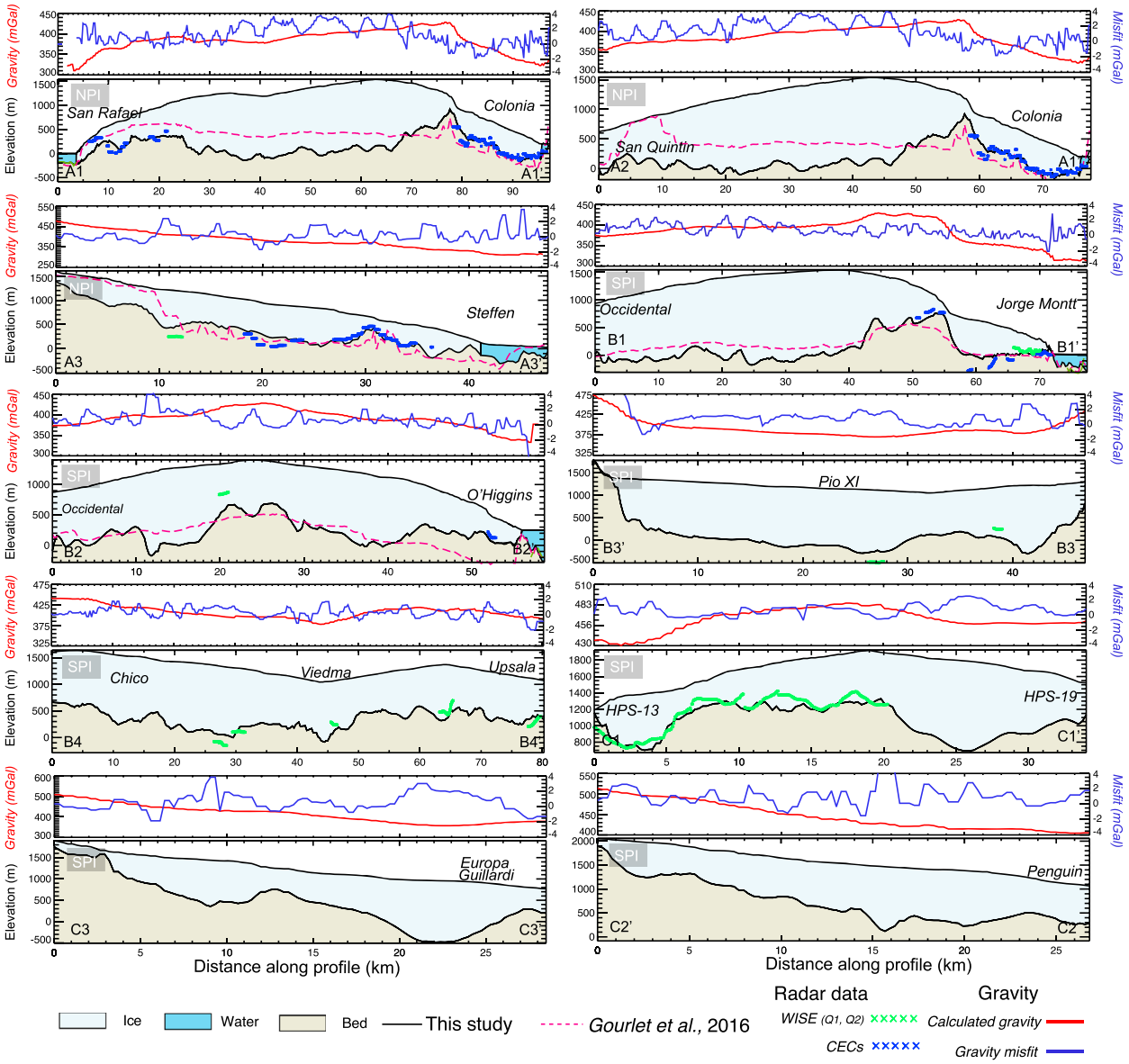

Figure 3. TanDEM-X/SRTM surface elevation along the profiles in Figure 2 with bed elevation above mean sea level inferred from gravity data (solid black), Gourlet et al. (2016) (dotted pink), radar sounder data from WISE (dotted green) and CECs (dotted blue). Water is blue, ice is light blue, and bed is light brown. NPI = Northern Patagonia Icefield; SPI = Southern Patagonia Icefield.

We interpret these differences as resulting from uncertainties in the simplified flow model approach of Carrivick et al. (2016) where ice thickness is estimated from surface slope along the centerline of each glacier.

The total ice volume for the surveyed sector of NPI is 974 ± 148 km^3 over an area of 2,358 km^2 or 57% of NPI (associated error is function of the sum of random errors on the ice thickness measurements). For SPI, the ice volume is 2,825 ± 403 km^3, over an area of 6,444 km^2 or 60% of SPI, for a combined total of 3,800 ± 554 km^3 over an area of 8,801 km^2 or 60% of NPI and SPI combined. To estimate the total ice volume of the Patagonia Icefields, we combine our results with Carrivick et al. (2016) outside of the survey area. For Upsala, Viedma and San Quintin glaciers, we adjust Carrivick et al. (2016) ice thickness downward with offsets varying between 200 and 300 m at the boundary to allow for a smooth transition (Figure S8). We calculate a total ice volume of 1,124 ± 260 km^3 for NPI and 3,632 ± 675 km^3 for SPI, for a combined total of 4,756 ± 935 km^3, which is 804 km^3 lower than Carrivick et al. (2016), or 15%. Hence, the gravity survey captured 86% of the total volume for NPI and 77% for SPI. For comparison, the ice volume in central Europe is 130 ± 30 km^3 or 36 times less that the ice volume in Patagonia (Huss & Farinotti, 2012).

We compare our volume estimate with the recent estimate of Farrinotti et al. (2019). Their value of 4,607 ± 1.2 km^3 for NPI and SPI is within error bars of our results, but their mapping does not capture major topographic features of the NPI and SPI, underestimates its deepest glacial valleys, with differences up to 1,000 m in San Quíntin, Colonia, Jorge Montt, and Occidental, and 106 ± 258 m on average (Figures 2 and S9). The agreement between the two total ice volumes is therefore more of a coincidence than a validation of the model results.

The largest reserves of ice are found along north-south troughs, which align well with the tectonic setting of this part of the Andes (Georgieva et al., 2016; Suarez & de la Cruz, 2000), for example, beneath San Rafael and Colonia or O'Higgins and Upsala. The other deep basins are oriented east-west along fjords and valleys. The fact that the northern NPI hosts more ice than the rest of Patagonia may be related to how tectonic raises the northern block compared to the southern block (Georgieva et al., 2016).

Over the next century, NPI and SPI are expected to increase their rapid contribution to sea level (Braithwaite & Raper, 2002; Gardner et al., 2013; Glasser et al., 2011; Levermann et al., 2013), enhanced hazards from glacial lake outburst floods (Anacona et al., 2015; Dussaillant et al., 2009; Loriaux & Casassa, 2013), and issues with freshwater resource management. From our product, the largest potential for sea level change exist for San Rafael and San Quintin in NPI, Jorge Montt, Pio XI, Occidental, O'Higgins, and possibly Upsala in SPI.

Our results that combines gravity and radar data provide a modicum of ground truth to evaluate techniques of glacier thickness mapping, for example, volume-area scaling (Bahr et al., 2015), slope-dependent models (Gartner-Roer et al., 2014), or simpler models (Farinotti et al., 2019). Our assessment indicates that these simplified approaches, which do not take into account ice velocity, have limited value to reveal the precise details of the bed topography beneath the icefields. To extend our results to lower elevation, we recommend using a mass conservation method combining ice flow vectors (Mouginot & Rignot, 2015), surface mass balance models (Lenaerts et al., 2014; Schaefer et al., 2015), and changes in surface elevation (Braun et al., 2019) as done successfully for ice sheets (Morlighem et al., 2014), mountain glaciers and ice fields (Rabatel et al., 2018).

This study demonstrates the usefulness of high-resolution airborne gravity surveys to constrain ice thickness and bed elevation in challenging glaciological settings, provided that independent observations exist to constrain the gravity inversion, for example, bathymetry, sparse radar-derived thickness, or seismic surveys (Rott et al., 1998). Gravity surveys are possible on fixed-wing airplanes, over the accumulation plateau of the icefields, with a 1- to 2-km line spacing, ground speed of 100 knots, and low clearance above the ice surface. In Patagonia, we found the best flying conditions in winter, when wind speeds are low. Shorter days and colder air temperature did not affect the survey performance or pilot safety margin.

5. Conclusions

The NPI and SPI are the largest ice mass in the Southern Hemisphere outside Antarctica, but a detailed description of the spatial distribution of its ice thickness has eluded observations. We demonstrate that high-resolution, high-quality, gravity data from an airborne platform, combined with sparse independent data, help provide the first, comprehensive, reliable view of the icefield thickness and bed elevation. While the resulting estimates of ice volume do not differ markedly from recent estimates, the bed topography and ice thickness products are more reliable and adapted for applications that require spatial details such as studies of glacier dynamics, glacial lake outburst, and evaluations of the sea level contribution. With more observations from radar sounders, seismic surveys and lake/fjord bathymetry, the inversion for ice thickness will continue to improve. In the mean time, the current bed topography and ice thickness data sets, that includes bathymetry in lakes and fjords, should make it possible, for the first time, to conduct detailed quantitative studies of the evolution of the major glaciers of Patagonia in a warming climate (e.g., Collao-Barrios et al., 2018)

Acknowledgments
This work was performed at the University of California Irvine, under grant 3280 from the Gordon and Betty Moore Foundation, at the Jet Propulsion Laboratory, California, Institute of Technology under grant NNX17AI02G with NASA Cryosphere Science, and at CECs under a grant from the Chilean National Science Fundation FONDECYT 1171832 and basal fund programs. We thank the helicopter pilots of the 2012 gravity survey conducted from Cochrane and Laguna San Rafael, the pilots of the 2014 radar and 2016 gravity survey conducted from Villa O'Higgins, the inhabitants of Villa O'Higgins for their hospitality, and the technicians and personal from Sanders Geophysics, Ltd. for their professional services. The gravity data from 2012 and 2016 and bed topography results from this study are available as Operation IceBridge data products at the National Snow and Ice Data Center, Boulder, CO. Other data are available upon request from the authors. The data are available on the UC dash system (https://doi.org/10.7280/D11Q17).

References

An, L., Rignot, E., Elieff, S., Morlighem, M., Millan, R., Mouginot, J., et al. (2017). Bed elevation of Jakobshavn Isbrae, west Greenland, from high-resolution airborne gravity and other data. *Geophysical Research Letters*, *44*, 3728–3736. https://doi.org/10.1002/2017GL073245

An, L., Rignot, E., Millan, R., Tinto, K., & Willis, J. (2019). Bathymetry of northwest Greenland using ocean melting Greenland (OMG) high-resolution airborne gravity and other data. *Remote Sensing*, *11*(2), 2072–4292.

Anacona, P. I., Mackintosh, A., & Norton, K. (2015). Reconstruction of a glacial lake outburst flood (GLOF) in the Engaño Valley, Chilean Patagonia: Lessons for GLOF risk management. *Science of The Total Environment*, *527–528*, 1–11.

Bahr, D. B., Pfeffer, W. T., & Kaser, G. (2015). A review of volume-area scaling of glaciers. *Reviews of Geophysics*, *53*, 95–140. https://doi.org/10.1002/2014rg000470

Blindow, N., Salat, C., & Casassa, G. (2012). Airborne GPR sounding of two deep temperate glaciers in the Northern Patagonia Icefield, *Proceedings of the 14th International Conference on Ground Penetrating Radar (GPR 2012)* (pp. 664–669). Shanghai, China: Tongji University.

Braithwaite, R. J., & Raper (2002). Raper glaciers and their contribution to sea level change. *Physics and Chemistry of the Earth*, *27*(32-34), 1445–1454.

Braun, M., Malz, P., Sommer, C., Farias Barahona, D., Sauter, T., Casassa, G., et al. (2019). Constraining glacier elevation and mass changes in South America. *Nature Climate Change*, *9*, 130–136.

Carrivick, J. L., Davies, B. J., James, W. H. M., Quinceya, D. J., & Glasserc, N. F. (2016). Distributed ice thickness and glacier volume in southern South America. *Global and Planetary Change*, *146*, 122–132.

Casassa, G., Kilian, R., Arévalo, M., Dietrich, R., Wendt, J., Wendt, A., et al. (2007). *Lago O'Higgins, Patagonia: Glacial over deepening and glacier retreat in a freshwater fjord*. Valdivia, Chile: Geosur.

Collao-Barrios, G., Gillet-Chaulet, F., Favier, V., Casassa, G., Berthier, E., Dussaillant, I., et al. (2018). Ice-flow modelling to constrain the surface mass balance and ice discharge of San Rafael Glacier, Northern Patagonia Icefield. *Journal of Glaciology*, *64*(246), 568–582.

Davies, B., & Glasser, N. (2012). Accelerating shrinkage of Patagonian glaciers from the Little Ice Age (∼AD 1870) to 2011. *Journal of Glaciology*, *58*(212), 1063–1084. https://doi.org/10.3189/2012JoG12J026

Dowdeswell, J. A., & Vasquez, M. (2013). Submarine landforms in the fjords of southern Chile: Implications for glacimarine processes and sedimentation in a mild glacier-influenced environment. *Quaternary Science Reviews*, *64*, 1–19.

Dussaillant, A., Benito, G., Buytaert, W., Carling, P., Meier, C., & Espinoza, F. (2009). Repeated glacial-lake outburst floods in Patagonia: An increasing hazard? *Natural Hazards*, *54*, 469–481.

Farinotti, D., Huss, M., Fürst, J., Landmann, J., Horst, M., Maussion, F., & Pandit, A. (2019). A consensus estimate for the ice thickness distribution of all glaciers on Earth. *Nature Geoscience*, *12*, 1752–0908.

Foresta, L., Gourmelen, N., Weissgerber, F., Nienow, P., Williams, J. J., Shepherd, A., et al. (2018). Heterogeneous and rapid ice loss over the Patagonian ice fields revealed by CryoSat-2 swath radar altimetry. *Remote Sensing of Environment*, *211*, 441–455.

Gardner, A., Moholdt, G, Cogley, J. G., Wouters, B., Arendt, A. A., Wahr, J., et al. (2013). A reconciled estimate of glacier contributions to sea level rise: 2003 to 2009. *Science*, *340*, 852.

Gartner-Roer, I., Naegeli, K., Huss, M., Knecht, T., Machguth, H., & Zemp, M. (2014). A database of worldwide glacier thickness observations. *Global and Planetary Change*, *122*, 330–344.

Georgieva, V., Melnick, D., Schildgen, T. F., Ehlers, T. A., Lagabrielle, Y., Enkelmann, E., & Strecker, M. R. (2016). Tectonic control on rock uplift, exhumation, and topography above an oceanic ridge collision: Southern Patagonian Andes (47°S), Chile. *Tectonics*, *35*, 1317–1341. https://doi.org/10.1002/2016TC004120

Glasser, N. F., Harrison, S., Jansson, K. N., Anderson, K., & Cowley, A. (2011). Global sea-level contribution from the Patagonian Icefields since the Little Ice Age maximum. *Nature Geoscience*, *4*, 303.

Gourlet, P., Rignot, E., Rivera, A., & Casassa, G. (2016). Ice thickness of the northern half of the Patagonia Icefields of South America from high-resolution airborne gravity surveys. *Geophysical Research Letters*, *43*, 241–249. https://doi.org/10.1002/2015GL066728

Hodgson, D. A., Jordan, T. A., De Rydt, J., Fretwell, P. T., Seddon, S. A., Becker, D., et al. (2019). Past and future dynamics of the Brunt Ice Shelf from seabed bathymetry and ice shelf geometry. *The Cryosphere*, *13*, 545–556. https://doi.org/10.5194/tc-13-545-2019

Huss, M., & Farinotti, D. (2012). Distributed ice thickness and volume of all glaciers around the globe. *Journal of Geophysical Research*, *117*, F04010. https://doi.org/10.1029/2012JF002523

Koppes, M., Sylwester, R., Rivera, A., & Hallet, B. (2010). Sediment yields over an advance-retreat cycle of a calving glacier, Laguna San Rafael, North Patagonian Icefield. *Quaternary Research*, *3*, 84–95.

Lenaerts, J. T., van den Broeke, M. R., van Wessem, J. M., van de Berg, W. J., van Meijgaard, E., van Ulft, L. H., & Schaefer, M. (2014). Extrem precipitation and climate gradients in Patagonia revealed by high-resolution regional atmospheric climate modeling. *Journal of Climate*, *27*, 4607–4621.

Levermann, A., Clark, P., Marzeion, B., Milne, G., Pollard, D., Radic, V., & Robinson, A. (2013). The multimillennial sea-level commitment of global warming. *Proceedings of the National Academy of Sciences of the United States of America*, *110*(34), 13,745–13,750.

Loriaux, T., & Casassa, G. (2013). Evolution of glacial lakes from the Northern Patagonia Icefield and terrestrial water storage in a sea-level rise context. *Global and Planetary Change*, *102*, 33–40.

Millan, R., Rignot, E., Bernier, V., Morlighem, M., & Dutrieux, P. (2017). Bathymetry of the Amundsen Sea Embayment sector of West Antarctica from Operation IceBridge gravity and other data. *Geophysical Research Letters*, *44*, 1360–1368. https://doi.org/10.1002/2016GL072071

Millan, R., Rignot, E., Mouginot, J., Wood, M., Bjork, A. A., & Morlighem, M. (2018). Vulnerability of Southeast Greenland glaciers to warm Atlantic Water from Operation IceBridge and Ocean Melting Greenland data. *Geophysical Research Letters*, *45*, 2688–2696. https://doi.org/10.1002/2017GL076561

Morlighem, M., Rignot, E., Mouginot, J., Seroussi, H., & Larour, E. (2014). Deeply incised submarine glacial valleys beneath the Greenland ice sheet. *Nature Geoscience*, *7*, 418–422.

Mouginot, J., & Rignot, E. (2015). Ice motion of the Patagonian Icefields of South America: 1984–2014. *Geophysical Research Letters*, *42*, 1441–1449. https://doi.org/10.1002/2014GL062661

Mouginot, J., Rignot, E., Gim, Y., Kirchner, D., & Meur, E. (2014). Low-frequency radar sounding of ice in East Antarctica and southern Greenland. *Annals of Glaciology*, *55*(67), 138–146. https://doi.org/10.3189/2014AoG67A089

Muto, A., Peters, L. E., Gohl, K., Sasgen, I., Alley, R. B., Anandakrishnana, S., & Rivermana, K. L. (2016). Subglacial bathymetry and sediment distribution beneath Pine Island Glacier ice shelf modeled using aerogravity and in situ geophysical data: New results. *Earth and Planetary Science Letters*, *433*, 63–75.

Nouvel, J. F., Herique, A., Kofman, W., & Safaeinili, A. (2004). Radar signal simulation: Surface modeling with the Facet Method. *Radio Science*, *39*, RS1013. https://doi.org/10.1029/2003RS002903

Rabatel, A., Sanchez, O., Vincent, C., & Six, D. (2018). Estimation of glacier thickness from surface mass balance and ice flow velocities: A case study on Argentiere Glacier, France. *Frontiers in Earth Science*, *6*, 112.

Raymond, C. F., Neumann, T. A., Rignot, E., Echelmeyer, K., Rivera, A., & Casassa, G. (2005). Retreat of Glaciar Tyndall, Patagonia, over the last half-century. *Journal of Glaciology*, *51*(173), 239–247.

Rees, W. G. (1990). *Physical principles of remote sensing*. New York: Cambridge University Press.

Rignot, E., Mouginot, J., Larsen, C. F., Gim, Y., & Kirchner, D. (2013). Low frequency radar sounding of temperate ice masses in Southern Alaska. *Geophysical Research Letters*, *40*, 5399–5405. https://doi.org/10.1002/2013GL057452

Rignot, E., Rivera, A., & Casassa, G. (2003). Contribution of the Patagonia Icefields of South America to sea level rise. *Science*, *302*(5644), 434–437.

Rivera, A., & Casassa, G. (2002). Ice thickness measurements on the Southern Patagonia Icefield. In G. Casassa, F. Sepulveda, & R. Sinclair (Eds.), *The Patagonian Icefields: A unique laboratory for environmental and climate change studies* (pp. 101–115), Series of the Centro de Estudios Cientificos. New York: Springer.

Rivera, A., Koppes, M., Bravo, C., & Aravena, J. C. (2012). Little Ice Age advance and retreat of Glaciar Jorge Montt, Chilean Patagonia. *Climate of the Past*, *8*, 403–414.

Rott, H., Stuefer, M., Siegel, A., Skvarca, P., & Eckstaller, A. (1998). Mass fluxes and dynamics of Moreno Glacier, Southern Patagonia Icefield. *Geophysical Research Letters*, *25*(9), 1407–1410.

Schaefer, M., Machguth, H., Falvey, M., Casassa, G., & Rignot, E. (2015). Quantifying mass balance processes on the Southern Patagonia Icefield. *The Cryosphere*, *9*, 25–35.

Suarez, M., & de la Cruz, R. (2000). Tectonics in the eastern Central Patagonian Cordillera (45°30′–47°30′S). *Journal of the Geological Society of London*, *157*, 995–1001.

Tinto, K. J., & Bell, R. E. (2011). Progressive unpinning of Thwaites Glacier from newly identified offshore ridge: Constraints from aerogravity. *Geophysical Research Letters*, *38*, L20503. https://doi.org/10.1029/2011GL049026

Ulaby, F. T., Moore, R. K., & Fung, A. K. (1982). *Microwave remote sensing*. Reading, Mass: Addison-Wesley-Longman.

Willis, M. J., Melkonian, A. K., Pritchard, M. E., & Rivera, A. (2012). Ice loss from the Southern Patagonian Ice Field, South America, between 2000 and 2012. *Geophysical Research Letters*, *39*, L17501. https://doi.org/10.1029/2012GL053136

Wood, M., Rignot, E., Fenty, I., Menemenlis, D., Millan, R., Morlighem, M., et al. (2018). Ocean-induced melt triggers glacier retreat in Northwest Greenland. *Geophysical Research Letters*, *45*, 8334–8342. https://doi.org/10.1029/2018GL078024

Zamora, R., & Uribe, J. (2017). Ice thickness surveys of the Southern Patagonian Ice Field using a low frequency ice penetrating radar system. In *First IEEE International Symposium of Geoscience and Remote Sensing (GRSS-CHILE)*, Valdivia, Chile.